

# Strong Adhesion and Friction Coupling in Hierarchical Carbon Nanotube Arrays for Dry Adhesive Applications

Shihao Hu,<sup>†</sup> Zhenhai Xia,<sup>\*,†,‡</sup> and Xiaosheng Gao<sup>†</sup>

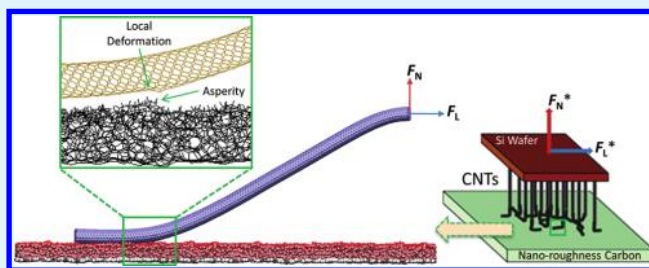
<sup>†</sup>Department of Mechanical Engineering, University of Akron, Akron, Ohio 44325, United States

<sup>‡</sup>Department of Materials Science and Engineering, Department of Chemistry, University of North Texas, Denton, Texas 76203, United States

**S** Supporting Information

**ABSTRACT:** The adhesion and friction coupling of hierarchical carbon nanotube arrays was investigated with a hierarchical multiscale modeling approach. At device level, vertically aligned carbon nanotube (VA-CNT) arrays with laterally distributed segments on top were analyzed via finite element methods to determine the macroscopic adhesion and friction force coupling. At the nanoscale, molecular dynamics simulation was performed to explore the origin of the adhesion enhancement due to the existence of the laterally distributed CNTs. The results show interfacial adhesion force is drastically promoted by interfacial friction force when a single lateral CNT is being peeled from an amorphous carbon substrate. By fitting with experiments, we find that under shearing loadings the maximum interfacial adhesion force is increased by a factor of  $\sim 5$ , compared to that under normal loadings. Pre-existing surface asperities of the substrate have proven to be the source of generating large interfacial friction, which in turn results in an enhanced adhesion. The critical peeling angles derived from the continuum and nano- levels are comparable to those of geckos and other synthetic adhesives. Our analysis indicates that the adhesion enhancement factor of the hierarchically structured VA-CNT arrays could be further increased by uniformly orienting the laterally distributed CNTs on top. Most importantly, a significant buckling of the lateral CNT at peeling front is captured on the molecular level, which provides a basis for the fundamental understanding of local deformation, and failure mechanisms of nanofibrillar structures. This work gives an insight into the durability issues that prevent the success of artificial dry adhesives.

**KEYWORDS:** adhesion, friction, carbon nanotube, dry adhesive, buckling, modeling



## 1. INTRODUCTION

Geckos can cling and maneuver on almost any kinds of surfaces,<sup>1</sup> whether smooth or rough, hydrophilic or hydrophobic, vertical or inverted. The extraordinary locomotion ability of geckos stems from the fine hairy structures of their footpads,<sup>2–7</sup> consisting of millions of micrometer-size fibril tissues, namely setae, which further split into 100–1000 nm-size branches, called spatulae. This unique hierarchical fibrillar structure allows for intimate contact with various target surfaces, generating formidable adhesive forces via intermolecular interaction.<sup>8–14</sup> Recently extensive efforts have been made to fabricate dry adhesives mimicking gecko footpad structures.<sup>15–17</sup> Vertically aligned carbon nanotube (VA-CNT) arrays have been demonstrated as a promising candidate due to its superior structural and mechanical properties.<sup>18–26</sup> Compared with their counterpart (i.e., polymeric patterns of micro/nano fibers<sup>27–36</sup>), VA-CNT arrays comprise densely packed high aspect ratio ( $\sim 10\,000:1$ ) CNTs with nanosized ultimate contacting elements (1–2 orders smaller than the size of gecko spatulae), which is crucial in achieving high interfacial adhesive strength based on the “contact splitting principle”.<sup>5,37,38</sup>

A recent breakthrough was led by the creation of hierarchically structured VA-CNT arrays.<sup>39</sup> Curly entangled segments (mimicking spatulae) laterally distributed on top of a straightly aligned body (similar to setae) enables a readily formalization of CNT side contacts when applied to a target surface.<sup>40</sup> Macroscopically, this two-level gecko-foot-mimetic CNT patch renders a frictional force of  $\sim 100\text{ N/cm}^2$ , about 10 times that a gecko can achieve in shear, and a low adhesion force of  $\sim 10\text{ N/cm}^2$  in normal direction. This adhesive force anisotropy ensures a strong binding on along the shear direction and easy lifting off in the normal direction. It is expected that the curly entangled segments on top play a crucial role in regulating the adhesion and friction at the nanoscale contact interface. Moreover, investigating the interfacial adhesion and friction forces and their effects on CNT peeling is essential for elucidating the local contact deformation and premature failure of the fibrillar-like materials, which determines the durability of artificial dry adhesives. In these regards, the interfacial behaviors of the hierarchically structured

**Received:** December 18, 2011

**Accepted:** March 9, 2012

**Published:** March 9, 2012

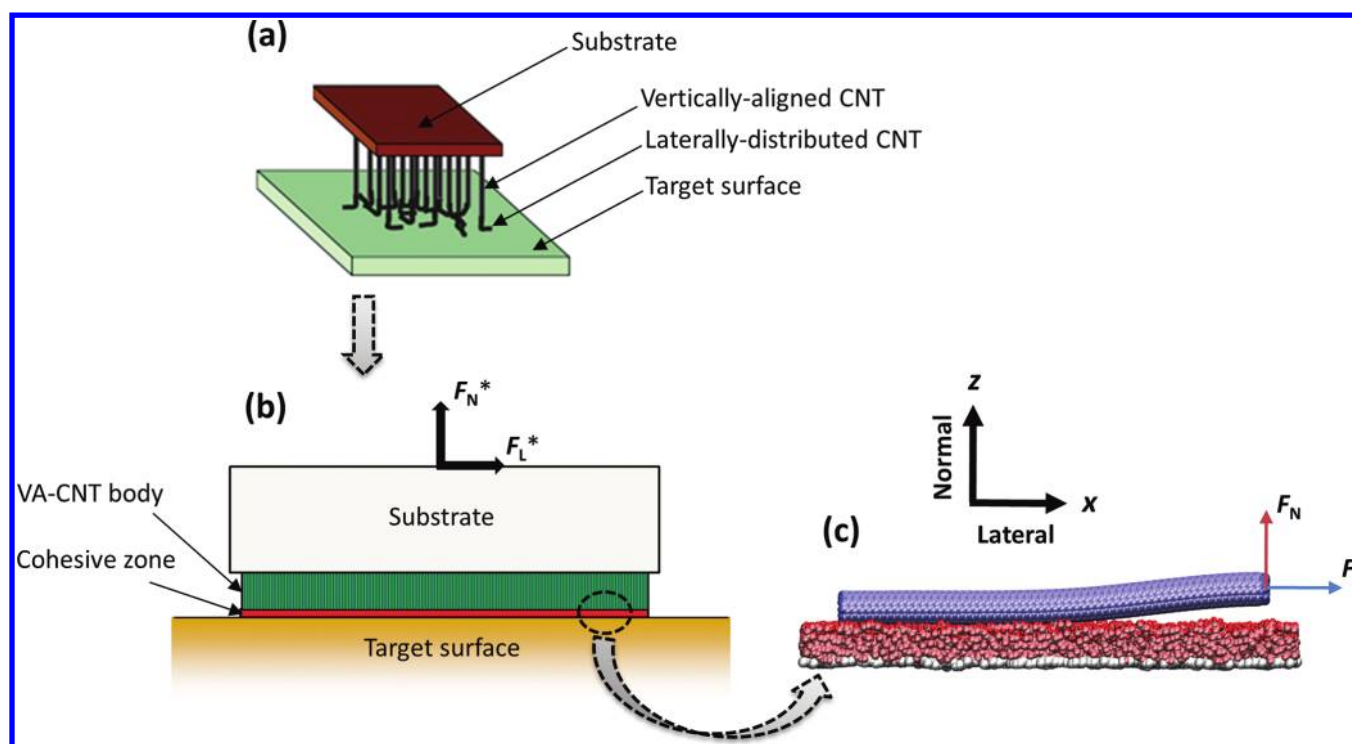


**Figure 1.** Schematics of (a) VA-CNT array with laterally distributed CNT segments adhering on a target surface and (b) FEA model for simulating the macroscopic adhesive behaviors of VA-CNT array. (c) Snapshot of a lateral CNT being peeled from a-C substrate in MD. Purple tube represents CNT, red beads represent saturating hydrogen atoms, pink beads represent a-C substrate, and white beads represent fixed carbon atoms at the bottom layer.

VA-CNT arrays were analyzed at different length scales. At the device level, finite element analysis (FEA) model with a cohesive zone at the interface was developed to predict interfacial failure and adhesive forces of the VA-CNT arrays. At the nanoscale, molecular dynamics (MD) simulation was performed to study the peeling behaviors of a single laterally distributed CNT from an amorphous carbon (a-C) substrate. By fitting the FEA models to the experimental data at the device level, we show that interfacial friction can enhance adhesion force by a factor of  $\sim 5$ . We also demonstrate via MD that the adhesion and friction forces are highly coupled when peeling individual lateral CNT segments from a substrate with nanoroughness. An analytical model was then developed which correlates adhesion force with friction force at the nanoscale interface. This work motivates a direction of designing high-performance CNT based dry adhesives for mimicking live gecko walking.

## 2. METHODOLOGY

The adhesion and friction behaviors of hierarchical VA-CNT arrays at macroscopic and atomistic length scales were simulated using two types of models, as shown in Figure 1. The macroscopic model for the VA-CNT arrays (Figure 1a) is a FEA model with a cohesive zone (Figure 1b), while the atomistic model described by fully atomistic MD consists of individual CNTs in side contact with a-C substrate (Figure 1c). The macroscopic model has the same size and configurations as the experimental samples ( $4 \times 4 \text{ mm}^2$ ).<sup>39</sup> The MD model simulates a single laterally distributed CNT segment on the hierarchical VA-CNT arrays.

**Finite Element Analysis.** Two-dimensional FEA featured with a cohesive zone was implemented using the Abaqus 6.8–2 software package. The details of this FEA model can be found in our recent publication.<sup>41</sup> Briefly, the model consists of four parts: substrate, VA-CNTs body, cohesive zone (interface between laterally distributed

CNT segments and target surface) and target surface, as schematically shown in panels a and b in Figure 1. The interfacial adhesion and friction behaviors at the device level were treated as the fracture resistance of a cohesive layer between the VA-CNT body and target surface. It has been demonstrated that the collective interactions between the laterally distributed CNTs and target surface can be described by distinctive bilinear traction-separation laws (cohesive laws),<sup>41</sup> as follows

$$T_N = \frac{T_N^i}{\delta_N^i} \delta_N \text{ when } 0 \leq \delta_N \leq \delta_N^i$$

$$T_N = \frac{T_N^i}{\delta_N^f - \delta_N^i} (\delta_N^f - \delta_N) \text{ when } \delta_N^i < \delta_N \leq \delta_N^f \quad (1)$$

where the subscript “N” refers to “normal direction”, the superscripts “i” and “f” refer to “damage initiation point” and “damage finishing point”, such that  $T_N^i$  designates the normal cohesive strength,  $\delta_N^i$  designates the normal displacement jump between two cohesive surfaces when damage initiates, and  $\delta_N^f$  designates the normal displacement jump when separation completes. Likewise the traction-separation law in lateral direction takes the same form as the pairwise eq 1 with the subscript “N” being substituted by “L”. So, there are in total six coefficients for the cohesive laws.

In our simulation, the  $\delta_N^i$  and  $\delta_L^i$  was controlled by  $E = T_N^i / \delta_N^i$  and  $G = T_L^i / \delta_L^i$ , respectively.  $\delta_N^f = \delta_L^f = 3 \text{ }\mu\text{m}$ ,  $E = 0.5 \text{ MPa}/\mu\text{m}$  and  $G = 2.0 \text{ MPa}/\mu\text{m}$  were taken in the simulation.  $T_N^i$  and  $T_L^i$  were obtained by matching the experimental results. In doing so, two provisional values for  $T_N^i$  and  $T_L^i$ , together with other four fixed coefficients, were loaded into an initial FE input file, run in Abaqus, and normal and shear force data were extracted from the FE output files. Adjustments to the coefficients were then made to reduce the error between experimental and FEA values.

Notably, the cohesive zone features distinct traction–separation relations in pure normal and pure lateral directions, where a layer of cohesive elements serve as an interface/path for crack initiation and

propagation. Using this approach, the empirical dependency between interfacial adhesion and friction forces, which are represented by the normal and shear cohesive strengths respectively, could be easily deduced by fitting with the experiment data because adjusting the cohesive law parameters in one direction would not disturb the other. In this phenomenological model, possible energy dissipation mechanisms in the VA-CNT body, such as the slightly unbuckling process and/or viscoelastic properties, will be implicitly reflected in the cohesive parameters that are calibrated with experimental data. Thus, the vertical CNT segments are modeled as an ideal elastic system.

**Fully Atomistic Molecular Dynamics Simulation.** The systems in MD simulation are composed of a single walled carbon nanotube (SWCNT) adhering to an a-C substrate (Figure 1c). SWCNTs in armchair configurations T (6, 6) were generated with the graphitic C–C bond length of 0.142 nm. SWCNTs with diameter of  $d = 0.81$  nm and lengths of  $L = 15$ – $60$  nm were used in the calculations. a-C substrates of  $\sim 2.4$  nm in width,  $\sim 1.5$  nm in thickness and density  $\rho = 2.2$ – $2.4$  g/cm<sup>3</sup> were created by melting diamond preforms at 7000 K and subsequently quenching into 0.5 K. In order to produce truly nonpolar dispersive surfaces, the a-C substrates were then saturated by hydrogen atoms and fully relaxed. After that, SWCNTs were put on the top of the substrate to make an initial side contact. Finally the whole system was fully relaxed at 0.5 K. The length of the a-C substrate is larger than each of the corresponding SWCNTs so that the entire contact interface undergoes peeling and sliding within the substrate.

Classical MD method was employed to simulate SWCNT peeling via LAMMPS simulator, by holding the two carbon rings at the right end of the CNT as a rigid body, moving upward with/without lateral constraints, achieving near equilibrium. With Langevin thermostat to control temperature, the equations of motion were integrated with a time step of 0.1 fs. To eliminate the possible effect of the thermostat on measured frictional force, we eliminated the thermostat coupling on the SWCNT and hydrogen atoms while the rest was still under the control of Langevin thermostat. Periodical boundary conditions were applied to the substrate in the length ( $x$ -) and width ( $y$ -) directions. The interactions between atoms were calculated using an AIREBO potential,<sup>42</sup> with a modified cutoff scheme.<sup>43</sup> This many-body potential has been frequently used to study the mechanical properties of carbon nanotubes and friction of diamond and amorphous carbon films.<sup>44–48</sup>

The Lennard–Jones (L–J) terms in the AIREBO was turned off; instead, a general L–J potential with a cutoff distance of 10 Å was introduced between the SWCNT and a-C substrate such that chemical bonding was avoided. The SWCNT/a-C interfacial interaction was then described only by the L–J potentials:  $U(r) = 4\epsilon[(r_0/r)^{12} - (r_0/r)^6]$  where the length  $r_0$  and energy  $\epsilon$  are 0.3465 nm and 2.86 meV for carbon, and 0.281 nm and 0.741 meV for hydrogen, respectively. The parameters for hydrogen–carbon interactions were obtained from the Lorentz–Berelot rules. As an explicit method, energy dissipation mechanisms such as viscoelasticity and buckling of CNTs were naturally included in the model.

### 3. RESULTS

**Adhesion Enhancement of Hierarchical VA-CNT Arrays at Device Level.** The maximum normal and lateral pulling forces ( $F_N^*$  and  $F_L^*$  in Figure 1b) that the VA-CNT pads can sustain when adhering to a target surface, were calculated with given sets of cohesive laws for different samples (different height of VA-CNTs body, Figure 1b). Obviously, the outputs of  $F_N^*$  and  $F_L^*$ , will depend on the coefficients of the input cohesive laws. There are 6 parameters ( $T_N^i$ ,  $\delta_N^i$ , and  $\delta_N^f$  in normal direction, and  $T_L^i$ ,  $\delta_L^i$ , and  $\delta_L^f$  in lateral direction) in the bilinear cohesive laws, designating the damage initiation and evolution of the cohesive elements in normal and lateral directions, respectively. We have previously studied the influence of  $\delta_N^i$  and  $\delta_L^i$  on the measured normal and lateral forces, and found that the effects of these parameters are trivial.<sup>41</sup> Similar results were obtained for the parameters,  $\delta_N^f$

and  $\delta_L^f$ . Thus, the cohesive strengths  $T_N^i$  and  $T_L^i$  are the dominant parameters in determining the macroscale adhesive forces (i.e.,  $F_N^*$  and  $F_L^*$ ) of the nanotube arrays. Because  $T_N^i$  and  $T_L^i$  are directly related to the laterally distributed CNT segments, the interfacial friction and adhesion behaviors of the lateral segments can be understood from FEA calculations. This provides an approach for evaluating the collective effects of the laterally distributed segments (i.e.,  $F_N$  and  $F_L$  in Figure 1c) and their contributions to the macroscopic properties (i.e.,  $F_N^*$  and  $F_L^*$  in Figure 1b).

We have calculated the normal cohesive strength (denoted as  $T_N^i(s)$ ) of the interface under shear loadings by adjusting the cohesive parameters of  $T_N^i$  and  $T_L^i$  simultaneously to match the experimental results of  $F_L^*$ .<sup>39</sup> Likewise, the normal cohesive strength (refers to  $T_N^i(n)$ ) of the interface under normal loadings was also calculated. The ratio of the normal cohesive strength under shear loading over that under normal loading ( $T_N^i(s)/T_N^i(n)$ ) is defined as the adhesion enhancement factor  $\phi^*$ , and shown in Figure 2 for samples with different VA-CNT

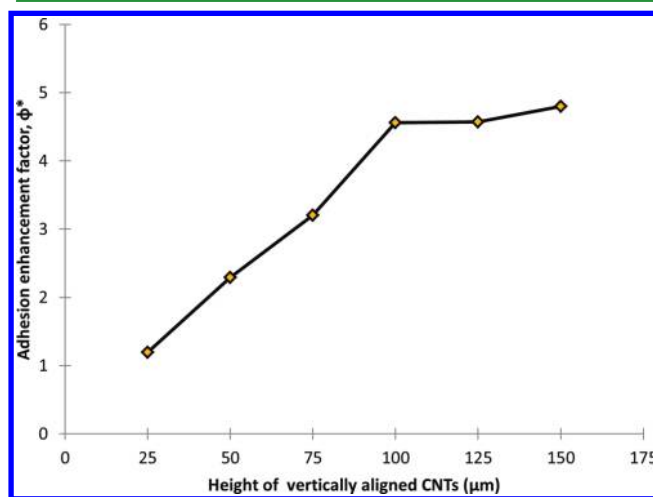


**Figure 2.** Adhesion enhancement factor  $\phi^*$  ( $T_N^i(s)/T_N^i(n)$ ) against the height of VA-CNT body, predicted by fitting FEA results to experimental data.

heights. With increasing the height of the vertically aligned CNT body, the enhancement factor increases and becomes constant ( $\sim 5$ ) after the height exceeds 100  $\mu\text{m}$ . However, we have also fitted FEA with the experimental results for VA-CNT arrays of different height without the laterally distributed CNT segments.<sup>39</sup> No such enhancement is found. Apparently, the enhancement of the adhesion forces under shear loadings is predominantly determined by the existence of the laterally distributed segments.

It should be clarified that, because of the pre-existing entangled top layer, the CNT side/line contacts readily forms once the adhesive patch is brought together with the target surfaces, without the need of inducing significant buckling of the vertical CNTs. Theoretically, the CNT side/line contacts will spontaneously occur when the two surfaces are close enough in the working range of intermolecular forces, especially on smooth surfaces like glass and silicon wafer. Besides, the density of CNT side/line contacts could not be significantly modified by increasing the preloading because of the crowding of the contacting elements at the interface and the parallel tube–tube interference between neighbors. During the experimental force measurements the compressive preloading



was a fixed value for each and every trial (i.e., a preload of about 2 kg) and was withdrawn before consecutive pulling tests were performed in either normal or shear directions. Hence, the initial contact fractions (i.e., CNT side/line contacts) before shear or normal loadings should be comparable, and does not contribute to the adhesion enhancement factors.

In the fitting process above, in addition to the pulling force ( $F_N^*$  and  $F_L^*$ ), the deformation of VA-CNT arrays was also matched up with the experimental results by adjusting the shear modulus of the vertical beams in FEA (modeling vertically aligned CNT stalks). The shear modulus is directly related to the fiber–fiber contact within VA-CNT arrays, which has been observed in the experiment.<sup>39</sup> Under shear loadings, the moment induced angles between the bended “CNT stalks” and target surface at the failure point of cohesive interface were measured and plotted in Figure 3. This angle is almost constant

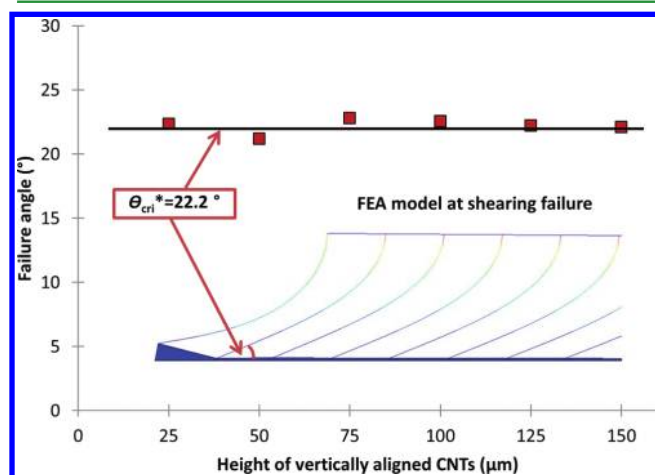


**Figure 3.** Failure angles of the hierarchical VA-CNT arrays with different heights of VA-CNT body under shear loadings in FEA simulation. A critical peeling angle of  $\theta_{\text{cri}}^* = 22.2^\circ$  is extracted from the experimental data through FEA. The inset illustrates a corresponding deformation of the VA-CNT array at interfacial failure.

with a value of  $22.2 \pm 0.6^\circ$  (average value  $\pm$  standard deviation) for different VA-CNT heights, indicating that it is independent of the geometry of CNT stalks. Because it was at the failure initiating point, the angle is defined as the critical peeling angle for interfacial failure,  $\theta_{\text{cri}}^*$ .

**Adhesion Enhancement of Individual CNTs at Nano-interface.** Aiming to assay the origin of the adhesion enhancement captured at the device level (Figure 2), we simulated the peeling of individual SWCNTs from an a-C substrate by pulling one end of the CNT upward in the direction normal to the substrate surface ( $z$ -direction in Figure 1c). For comparison, we studied two displacement controlled loading conditions: the lateral displacement of the CNT pulling end is (i) fixed (namely fixed peeling) or (ii) unfixed (i.e., free peeling) while it is pulled upward. In the fixed peeling, the pulling end of the CNT is fixed in lateral ( $x$ -) direction, similar to that in the CNT peeling experiments done by Ishikawa et al.<sup>49</sup> For the free peeling, the end is not fixed and can freely move in the  $x$ -direction.

Under the fixed peeling condition, after an initial peeling stage (not shown in Figure 4) at the pulling end (inset A in Figure 4a), both friction force ( $F_L$ ) and adhesion force ( $F_N$ ) gradually build up with a strong coupling effect. At this stage, the peeling occurs in a stick–slip manner and multiple peaks

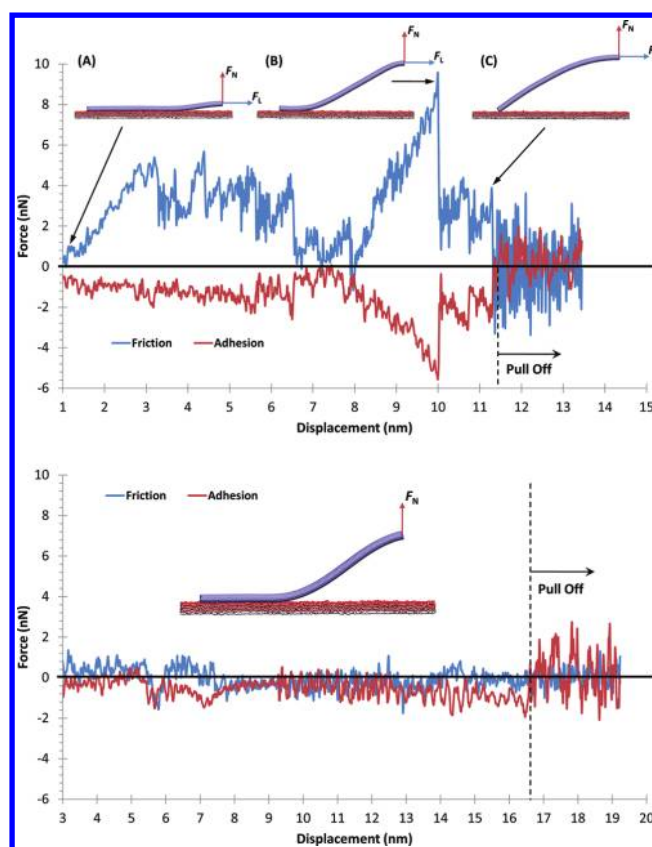


**Figure 4.** Friction and adhesion forces of 30 nm SWCNT during (a) fixed peeling and (b) free peeling. Insets in (a) are snapshots of the nanotube configurations at the points of (A) initial peeling, (B) peak force, and (C) pulling off. Inset in b is a snapshot of CNT free peeling, maintaining negligible frictional force.

can be seen on the force–pulling distance curves. These peaks occur randomly because of the rough nature of the substrate; their magnitude depends on local CNT–asperity interactions. Maximum friction and adhesion forces are achieved simultaneously at a point (inset B in Figure 4a). After a significant separation, the CNT configuration suddenly transforms from s- to arc-shape (inset C in Figure 4a), resulting in a rapid drop of the coupled forces. After this critical point, the edge of the other CNT end slides on the substrate, the coupling effect could also be observed but its value becomes much lower. Eventually, the SWCNT is pulled off from the substrate. These results well agree the experimental results on single CNT peeling.<sup>49</sup> However, the frictional force was not measured simultaneously in these experiments. Consequently, the important feature of peeling, frictional–adhesion coupling, was not observed. Nonetheless the normal force–distance curve obtained in our MD simulation is consistent with the experimental data available in the open literature. The friction–adhesion coupling captured by the MD simulation is similar to that observed in gecko footpads.<sup>50</sup>

The boundary conditions have a significant effect on the friction and adhesion peaks. For the 30 nm long SWCNT, maximum adhesion force synchronically achieves 5.67 nN when frictional force reaches its peak value of 9.54 nN (Figure 4a). In contrast, when the constraint of CNT pulling point in the lateral direction is set free, i.e., under free peeling boundary condition (inset of Figure 4b) where no force is applied in shear direction during peeling, the adhesion force drops to

much lower values ( $<2$  nN). There is neither distinguishable peak nor significant force coupling effect during free peeling, as shown in Figure 4b. Obviously, a substantially high adhesion force  $F_N$  is generated when high levels of friction force  $F_L$  exist, whereas it becomes significantly low in the case of low friction.

The effect of the lateral CNT length on the friction and adhesion forces ( $F_L$  and  $F_N$ ) was also analyzed and plotted in Figure 5. As the tube length increases, both of the maximum

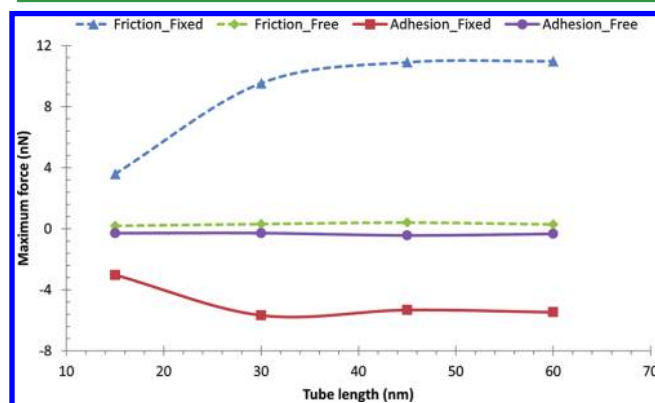


**Figure 5.** Maximum adhesion and friction forces as a function of SWCNT length under the fixed and free peeling conditions. Because there is no distinctive peaks and coupling effect during the free peeling (e.g., Figure 4b), average forces are taken instead of maximum values, which are roughly at the level of 0.2–0.5 nN in terms of adhesion forces.

forces increase and eventually reach a plateau under the fixed peeling condition. However, for the free peeling with negligible frictions, the maximum normal peeling force is independent of the tube length and its value is much lower ( $F_N \approx 0.5$  nN). This clearly demonstrates that frictional force can significantly enhance normal peeling force. There is a critical tube length beyond which the enhancement will level off. It is attributed to an additional bending moment imposed by the “fixed end” boundary condition, which tends to open the crack tip at peeling front. For a CNT shorter than the critical length (e.g., tube length = 15 nm), this additional bending moment strongly affects the CNT contact region, preventing the peeling forces to build up. However, this additional bending moment has a limited working distance (longitudinally  $\sim 20$  nm). For a longer CNT (tube length  $\geq 30$  nm), the peeling front quickly moves out of the working distance upon loading. High friction and adhesion can then develop. Since the achievable local friction force largely depends on the surface condition, rather than CNT length, increasing the tube length over the critical value cannot further increase the coupled reaction forces.

To quantitatively show the adhesion enhancement at this isolated “ideal case”, we define the ratio of the maximum adhesion force with friction over that without (or with negligible) friction as the nanoscale adhesion enhancement factor  $\phi$  (analogous to  $\phi^*$  in FEA). The maximum value of  $\phi$  reaches  $\sim 10$ , as extracted from Figure 5.

To further explore the enhancement mechanism, we plotted adhesion force against friction force in Figure 6 when the 30 nm tube undergoes fixed peeling. At zero friction there is an initial adhesion force of  $\sim 0.28$  nN. There is a large scattering of the data mainly due to the thermal fluctuation, but a roughly linear relationship between the adhesion and friction forces can be extracted with a slope of 0.5057. The angle associated with

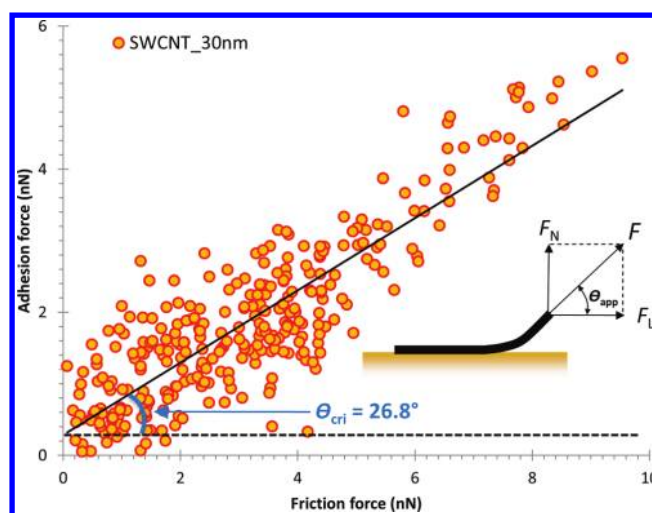


**Figure 6.** Adhesion force as a function of friction force for 30 nm long SWCNT under fixed peeling.  $\theta_{\text{cri}}$  is the averaged critical angle.  $\theta_{\text{app}}$  in the inset is the instantaneous angle of the reaction force,  $F$ , from the horizontal plane under displacement controlled peeling.

the forces applied in normal and shear directions is determined to be  $26.8^\circ$ . Because it was measured throughout the peeling process, the adhesion force corresponds to the critical peeling force that the CNT can sustain at a given frictional force. Hence, the angle extracted here represents a critical angle  $\theta_{\text{cri}}$  under which the adhesion enhancement is maximized. If the angle imposed by external loadings ( $\theta_{\text{app}}$  in the inset of Figure 6) exceeds this critical value the nanotube will be peeled off spontaneously.

It is noteworthy that the peeling angle  $\theta$  defined here indicates the instantaneous relationships between the normal and shear reaction forces ( $F_N/F_L$ ; adhesion force/friction force), when certain displacement controlled peeling is applied on one end of the tube. It is conceptually different from the peeling angle designated in the well-known Kendall model and the ones based on it,<sup>51–53</sup> where the peeling angle is defined as the angle between the peeling film and substrate. We have calculated the angles between the CNT and substrate for a long CNT (tube length  $>30$  nm), and compared it with that defined by the forces applied in normal and shear direction. We found that the peeling angle associated with the force is very close to that between CNT and substrate except for those at the initial peeling stage. The difference in peeling angles at the initial peeling stage is caused by the effect of the “fixed end” boundary conditions which alters the configuration of the CNT near the peeling end. As the peeling front moves out of the effective distance of the “fixed end”, the two angles merge. As will be discussed in section 4, the critical angle  $\theta_{\text{cri}}$  used here is intrinsically determined by the conditions of surface roughness at a corresponding scale. In contrast, Kendall elastic tape peeling model does not deal with the surface conditions of the contacting substrates because of its energy based nature.

We have calculated  $\theta_{\text{cri}}$  for different nanotube lengths (15–60 nm) and found that it is nearly constant ( $\theta_{\text{cri}} = 25.2 \pm 1.3^\circ$ ) on the substrates with the same levels of roughness. Interestingly, the critical angle calculated in MD simulation is very close to the value ( $24$ – $30^\circ$ ) found in gecko setal release.<sup>50</sup> Presumably, the orientations of angled setal stalks are evolved in such a geometrical setting that gages the adhesion by controlling friction under the influence of surface conditions

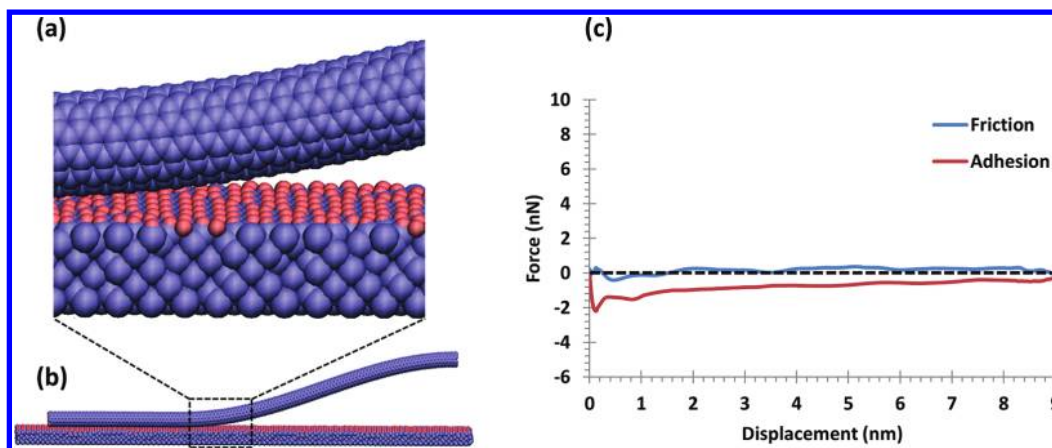


**Figure 7.** (a) Close view and (b) fair view of 30 nm long SWCNT, armchair T (6, 6), fixed peeling from an atomically smooth diamond substrate. Purple beads represent carbon atoms, red beads represent saturating hydrogen atoms. (c) Friction and adhesion forces of 30 nm SWCNT under fixed peeling from an atomically smooth diamond substrate.

(i.e., roughness) at micro/nanoscale. From the above analysis, we can establish an empirical relationship between the adhesion  $F_N$  and friction  $F_L$  forces as

$$F_N = F_O + \eta F_L \quad (2)$$

where  $F_O$  is the initial adhesion force, and  $\eta$  is the adhesive coefficient, which is the slope of the adhesion-friction curve or the tangent of critical peeling angle ( $\eta = \tan \theta_{\text{cri}}$ ).

For comparison, an atomically smooth diamond substrate was generated to replace the a-C substrate used in the MD simulations, as shown in Figure 7a, b. Figure 7c shows the friction and adhesion forces of the nanotube being peeled from an atomically smooth diamond substrate under the fixed peeling condition. With negligible frictional force, the adhesion force keeps lower than 2 nN, excluding the initial crack opening stage from the displacement of 0 to  $\sim 0.3$  nm, and there is no distinguishable coupling effect between the two forces. These results suggest that surface condition (i.e., roughness) is of great importance in adhesion enhancement.

#### 4. DISCUSSION

Both FEA and MD simulations demonstrate that there is a strong enhancement of adhesion force due to the presence of friction force on the laterally distributed CNT segments. The FEA with experimental fitting suggests that the adhesion force could be increased by a factor of  $\sim 5$ , while the MD calculation indicates that the maximum enhancement value reaches  $\sim 10$  for the SWCNT/a-C systems. Note that the interfacial behaviors predicted in FEA represent the collective effect of single laterally distributed CNT segments. Because the lateral segments on VA-CNT arrays distribute randomly in all directions,<sup>39</sup> free peeling of those lateral segments within an array is prevented even under pure normal pulling. Consequently, nontrivial amount of friction forces are generated, which in turn increase the adhesion forces under normal loadings. Thus, the enhancement factor that we derived at the device level is relatively small. However, the enhancement factor can be further optimized by making unidirectionally oriented lateral CNTs similar to that of gecko spatulae, so that upon normal pulling (in the releasing direction) most of the ultimate contacting elements could be peeled freely.

Obviously, there is a great advantage of utilizing atomistic molecular dynamics simulations to build the nanoscale peeling

systems atoms by atoms, and explicitly calculate the interaction force distributions at the interface along with the reaction forces at the pulling end for different boundary conditions. In this way the missing picture may be completed between the discrete and continuum scales, whenever an emphasis on the nanoscale phenomena is highly important.

The adhesion enhancement revealed here is the result of molecular interactions between CNT and a-C substrate. Usually for a fiber/elastic-tape being peeled from a substrate, three regions are classified as contact region (Region I), peeling zone (Region II) and peeled region (Region III), as shown in Figure 8a. The friction force (lateral force;  $F_L$ ) is generated because of the frictional contact in the contact region (Region I), whereas the adhesion force (normal force;  $F_N$ ) is attributed to van der Waals interaction between the fiber and substrate in the peeling zone (Region II).<sup>54</sup> The net normal force on the CNT is assumed to be zero in Region I and III. However, to achieve enhanced adhesion force, there must be a region in which extra normal force is generated by friction to balance the total applied load. We found that this particular region is located right in front of the peeling zone, namely adhesion-enhancing zone (Region IV as shown in Figure 8b). This region has a unique geometric feature, where the nanotube curves up, forming an upward slope upon a pre-existing asperity. This configuration could also be reinforced by sink-in of the nanotube into the substrate and pile-up of the substrate superficial atoms under the local adhesion and friction forces, given a relatively soft substrate. It has been identified that both of the aforementioned effects exist in our MD simulations with the former being more dominant. In either case, the slope will cause a resultant of local friction force in the normal direction ( $z$ -direction) due to the hindering effect of the asperity. Such friction resultant directly contributes to the resistance to the normal peeling force,  $F_N$ .

Figure 8b shows the tube axial strain, along with the height profiles of the CNT and that of the substrate contacting surface underneath the CNT, when adhesion and friction forces ( $F_N$  and  $F_L$ ) reach a peak. At this point, the axial strain in the contact region (Region I) is low but it jumps up to a higher level in the Region IV and become nearly constant in Regions II and III. The rapid change in strain reveals the existence of a large static frictional force on the nanotube in Region IV. Such a high frictional force is attributed to the mechanical interlock



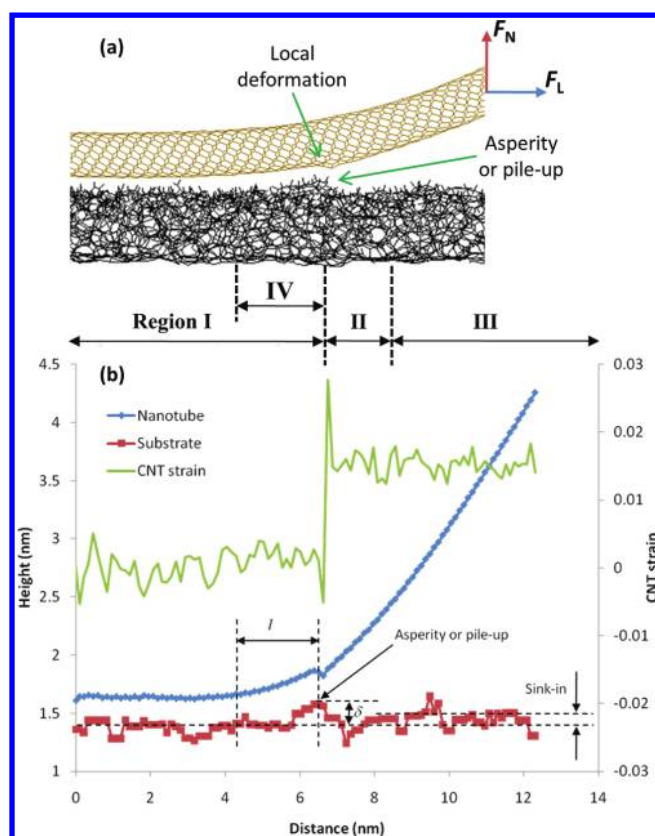


**Figure 8.** (a) Snapshot of nanotube peeling from a-C substrate with nanoscale roughness and asperities, showing different interfacial regions of tube-substrate interaction and local tube deformation. (b) CNT axial strain, height profiles of CNT and substrate near peeling region when the coupled adhesion and friction forces reach a peak for 30 nm SWCNT.

of the nanotube on a single asperity, which results in a severe local CNT deformation, as shown in Figure 8a. In fact, at the left side of the asperity (adhesion enhancing zone, Region IV), large lateral compressive force between the tube and sloping surface of the substrate are generated under fixed peeling conditions, because of the drastically increased Pauli repulsion of the particles having overlapping orbitals at short ranges. Such compressive force (or resisting force) is different from the van der Waals attractive force (dispersion force), which arises from the fluctuating polarizations of nearby particles and is relatively weak. As previously described, we have performed nanotube peeling from an atomically smooth diamond surface with hydrogen saturation under the same fixed peeling conditions (Figure 7). No such enhancing phenomenon is observed mainly because there is a lack of asperity on the flat diamond surface, which is also very dense and hard. Apparently proper asperities are necessary to generate large friction force and in turn large adhesion force. For the SWCNT/a-C systems in our MD simulations, the height of the single asperity is measured as  $\delta \approx 0.2$  nm, and the length of the adhesion-enhancing zone is  $l \approx 2$  nm.

Assuming that a single asperity hinders a CNT in adhesion-enhancing zone during peeling, we derived a theoretical

relationship linking adhesion to friction forces (see the Supporting Information)

$$F_N = \frac{Hl\sqrt{d}}{16D_0^{2.5}} \left( 1 + \tan^2 \theta + \frac{D_0}{1.5l \tan \theta} \right) + F_L \tan \theta \quad (3)$$

where  $H$  is the Hamaker constant,  $d$  is the nanotube diameter,  $D_0$  is the gap distance between the nanotube surface and substrate, and  $\theta$  is the tangential angle of the nanotube at the asperity. Since  $H$ ,  $d$ ,  $D_0$ ,  $l$  and  $\theta$  are constants for a given system, the adhesion force is proportional to friction force, exactly the same as eq 2 obtained from MD simulation, with  $F_0 = (Hl\sqrt{d})/(16D_0^{2.5})(1 + \tan^2 \theta + D_0/(1.5l \tan \theta))$ , and  $\eta = \tan \theta$ , which gives the critical angle  $\theta_{\text{cri}}$  a clear physical meaning.

We have estimated the initial adhesion  $F_0$  and the adhesive coefficient  $\eta$  from the theoretical relationship. Assuming that CNT deflection can be described by Timoshenko beam theory we have

$$\eta = \left( \frac{\delta}{l} \right) \left( \frac{1/2 + \lambda}{1/3 + \lambda} \right) \quad (4)$$

$$\lambda = \frac{(1 + \nu)(d_o^2 + d_i^2)}{8k^2 l^2} \quad (5)$$

where  $\lambda$  is a dimensionless parameter related to nanotube diameter  $d$  (subscripts “o” and “i” represent “outer” and “inner”, respectively) and Poisson ratio  $\nu$ , and the Timoshenko correction factor  $k$  ( $k \approx 0.638$  for circular cross-section). According to eqs 4 and 5, the adhesive coefficient depends largely on the nanotube geometry and surface roughness, rather than materials property. Taking the value of  $d_o = 0.97$  nm,  $d_i = 0.63$  nm,  $\nu = 0.19$ ,  $\delta = 0.2$  nm, and  $l = 2$  nm, we have  $\eta = 0.159$  or  $\theta = 9.0^\circ$ . The value is relatively low compared to the MD simulations, presumably resulted as the neglect of local CNT deformation at the asperity (Figure 8a). Accounting for the local deformation yields  $\eta = 0.368$  and  $\theta = 20.5^\circ$ , much closer to the MD results. Using the values<sup>39</sup> of  $H = 6 \times 10^{-20}$  J,  $D_0 = 0.34$  nm, we estimate  $F_0 = 0.26$  nN, which also agrees with the MD simulations. From these analyses, it is clear that the adhesion enhancement depends largely on the nanotube geometry, surface roughness, and local deformation.

As shown in eq 3, the adhesive coefficient  $\eta$  or the critical angle  $\theta_{\text{cri}}$  is an important factor in determining the adhesion enhancement. Notably, the moment induced failure angles  $\theta_{\text{cri}}^*$  between the bended “CNT stalks” and “substrate” (Figure 3) calculated from FEA is about  $22.2 \pm 0.6^\circ$  (average value  $\pm$  standard deviation). Such critical failure angle derived from the experiment and FEA is remarkably close to that obtained from the fully atomistic MD simulation at the nanoscale (Figure 6), implying the intrinsic enhancement mechanism when friction is present.

The adhesion enhancement factor for CNT systems is 5–10, calculated from FEA and MD simulations at different length scales. This enhancement factor could also be estimated by other types of analytical models such as energy-based Kendall’s model.<sup>51</sup> Although the geometrical conditions in Kendall’s peeling model are not the same as those in our multiscale simulations, it is justifiable to see if the predictions from the energy-based approach are consistent with the detailed force analysis for similar peeling processes. According to the definition, the adhesion enhancement factor  $\phi_k$  is the ratio of the normal peeling force with friction to that without friction.

From Kendall's model, the resultant peeling force in shear direction is zero for a peeling angle of  $\theta = 90^\circ$ . Thus, the enhancement factor can be determined as

$$\phi_k = \frac{\sin \theta \sqrt{1 + \frac{2\gamma}{EA}} + \sin \theta}{\sqrt{(1 - \cos \theta)^2 + \frac{2\gamma}{EA}} + 1 - \cos \theta} \quad (6)$$

where  $\gamma$  is the van der Waals interaction energy, and  $E$  and  $A$  are the Young's modulus and tape thickness, respectively. A simple analysis on eq 6 shows that there is a critical angle, at which  $\phi_k$  reaches a maximum value. Taking the value of  $A = d_o = 0.97$  nm,  $E = 500$  GPa, and  $\gamma = 0.3\text{--}0.4$  J/m<sup>2</sup>,<sup>21</sup> we estimate the maximum enhancement factor  $\phi_k = 6.1\text{--}6.6$ , very close to our results from FEA and MD simulations. Analysis via eq 6 also shows that the enhancement factor is a weak function of Young's modulus, which is consistent with our analysis. However, the critical angle ( $\sim 12^\circ$ ) predicted from Kendall model is quite lower than those obtained from FEA and MD simulation. More recently, a modified Kendall's peeling model has been proposed by introducing a pretension term.<sup>55</sup> The critical angles derived are much more consistent with our results. They show a  $\sim 26^\circ$  force-independent critical angle for gecko fibrillar structures when pretension makes the pull-off force plunges to zero.

Table 1 lists the critical angles and adhesion enhancement factors for various fibrillar materials, calculated from the

**Table 1. Parameters Calculated for the Adhesion Enhancement of Various Materials**

materials	critical angle (deg)	adhesion coefficient	enhancement factor
Gecko setal array <sup>50</sup>	24.6–30	0.430–0.597	20–29
Polypropylene fiber array <sup>56</sup>	15–24	0.268–0.445	9–11
MWCNT array <sup>39</sup>	21–24	0.383–0.445	2–5
Individual SWCNTs	25.2	0.468	$\sim 10$

experiments<sup>39,50,56</sup> and simulations. The critical angles are in a narrow range between  $20\text{--}30^\circ$  for the materials with completely different properties which agree with the predictions of the analytic models described above.

As shown in Table 1, among these fibrillar nanostructures, gecko setal arrays exhibit the highest adhesion enhancement ( $20\text{--}29$ ), whereas most synthetic materials have relatively small enhancement factors ( $<10$ ). According to our analysis (eqs 2–4), to achieve a large enhancement factor or force anisotropy in synthetic dry adhesives, it is important to reduce the initial adhesion force  $F_O$ , or increase the interfacial friction force  $F_L$ . This could be achieved by modifying the geometry and surface chemistry of the contacting layer (i.e., the laterally distributed segments in VA-CNT arrays). For example, mimicking gecko seta-spatula structure, one could make all the second-level CNT segments oriented in one direction instead of randomly distributed. When the hierarchical CNT arrays are peeled freely in the normal direction, the initial adhesion force  $F_O$  would be significantly reduced. As a result, the force anisotropy between the normal and shear directions could be further promoted.

## 5. CONCLUSIONS

The adhesion and friction behaviors of hierarchical VA-CNT arrays were analyzed at multiple length scales using FEA and

MD simulations. Results show that, with a second-level of hierarchy: laterally distributed CNT segments on top of VA-CNT arrays, the adhesion force could be enhanced by a factor of 5 and 10 at macro- and nanoscales, respectively. A molecular mechanism of interfacial adhesion enhancement due to the lateral CNTs was revealed, in which the adhesion force is strongly enhanced by interfacial friction because of pre-existing asperities on substrate. A linear adhesion–friction relationship was established based on MD simulations and theoretical analysis. The critical angles of the lateral CNT segments peeling from a-C substrate were calculated and the values are comparable to those for gecko and other synthetic adhesives. The analytic model predicts that the critical angle is mostly dependent on the fiber geometry and surface roughness but relatively insensitive to the material types and mechanical properties, which is consistent with experimental data published in open literatures. Our analysis at macro- and nanoscale indicates that properly orienting the ultimate contacting elements could further increase adhesion enhancement factor or force anisotropy of the hierarchical VA-CNT arrays. This work provides a basis for analyzing the deformation and failure mechanisms in the nanofibrillar structures, and sheds light on the durability issues that impede the success of artificial dry adhesives in general.

## ■ ASSOCIATED CONTENT

### Supporting Information

Theoretical derivations of adhesion enhancement at nanoscale contact. This material is available free of charge via the Internet at <http://pubs.acs.org/>.

## ■ AUTHOR INFORMATION

### Corresponding Author

\*E-mail: Zhenhai.Xia@unt.edu. Tel: 940-369-7673. Fax: 940-369-4824.

### Notes

The authors declare no competing financial interest.

## ■ ACKNOWLEDGMENTS

The authors acknowledge the support from NSF (CMMI-0825990), and AFOSR MURI (FA9550-12-1-0037).

## ■ REFERENCES

- (1) Autumn, K.; Gravish, N. *Philos. Trans. R. Soc. London, Ser. A* **2008**, *366*, 1575–1590.
- (2) Williams, E. E.; Peterson, J. A. *Science* **1982**, *215*, 1509–1511.
- (3) Russell, A. P. *Integr. Comp. Biol.* **2002**, *42*, 1154–1163.
- (4) Autumn, K.; Peattie, A. M. *Integr. Comp. Biol.* **2002**, *42*, 1081–1090.
- (5) Arzt, E.; Gorb, S.; Spolenak, R. *Proc. Natl. Acad. Sci. U.S.A.* **2003**, *100*, 10603–10606.
- (6) Gao, H. J.; Wang, X.; Yao, H. M.; Gorb, S.; Arzt, E. *Mech. Mater.* **2005**, *37*, 275–285.
- (7) Yao, H.; Gao, H. J. *Mech. Phys. Solids* **2006**, *54*, 1120–1146.
- (8) Irschick, D. J.; Austin, C. C.; Petren, K.; Fisher, R. N.; Losos, J. B.; Ellers, O. *Biol. J. Linn. Soc.* **1996**, *59*, 21–35.
- (9) Autumn, K.; Liang, Y. A.; Hsieh, S. T.; Zesch, W.; Chan, W. P.; Kenny, T. W.; Fearing, R.; Full, R. J. *Nature* **2000**, *405*, 681–685.
- (10) Autumn, K.; Sitti, M.; Liang, Y. C. A.; Peattie, A. M.; Hansen, W. R.; Sponberg, S.; Kenny, T. W.; Fearing, R.; Israelachvili, J. N.; Full, R. J. *Proc. Natl. Acad. Sci. U.S.A.* **2002**, *99*, 12252–12256.
- (11) Huber, G.; Gorb, S. N.; Spolenak, R.; Arzt, E. *Biol. Lett.* **2005**, *1*, 2–4.



- (12) Niewiarowski, P. H.; Lopez, S.; Ge, L.; Hagan, E.; Dhinojwala, A. *Plos One* **2008**, *3*, e2192.
- (13) Chen, B.; Gao, H. J. *Int. J. Appl. Mech.* **2010**, *2*, 1–9.
- (14) Puthoff, J. B.; Prowse, M. S.; Wilkinson, M.; Autumn, K. *J. Exp. Biol.* **2010**, *213*, 3699–3704.
- (15) Jeong, H. E.; Suh, K. Y. *Nano Today* **2009**, *4*, 335–346.
- (16) Boesel, L. F.; Greiner, C.; Arzt, E.; del Campo, A. *Adv. Mater.* **2010**, *22*, 2125–2137.
- (17) Sameoto, D.; Menon, C. *Smart Mater. Struct.* **2010**, *19*, 103001.
- (18) Kinoshita, H.; Kume, I.; Tagawa, M.; Ohmae, N. *Appl. Phys. Lett.* **2004**, *85*, 2780–2781.
- (19) Yurdumakan, B.; Raravikar, N. R.; Ajayan, P. M.; Dhinojwala, A. *Chem. Commun.* **2005**, 3799–3801.
- (20) Dickrell, P. L.; Sinnott, S. B.; Hahn, D. W.; Raravikar, N. R.; Schadler, L. S.; Ajayan, P. M.; Sawyer, W. G. *Tribol. Lett.* **2005**, *18*, 59–62.
- (21) Zhao, Y.; Tong, T.; Delzeit, L.; Kashani, A.; Meyyappan, M.; Majumdar, A. *J. Vac. Sci. Technol., B* **2006**, *24*, 331–335.
- (22) Qu, L.; Dai, L. *Adv. Mater.* **2007**, *19*, 3844–3849.
- (23) Aksak, B.; Sitti, M.; Cassell, A.; Li, J.; Meyyappan, M.; Callen, P. *Appl. Phys. Lett.* **2007**, *91*, 061906.
- (24) Ge, L.; Sethi, S.; Ci, L.; Ajayan, P. M.; Dhinojwala, A. *Proc. Natl. Acad. Sci. U.S.A.* **2007**, *104*, 10792–10795.
- (25) Wirth, C. T.; Hofmann, S.; Robertson, J. *Diamond Relat. Mater.* **2008**, *17*, 1518–1524.
- (26) Sethi, S.; Ge, L.; Ci, L.; Ajayan, P. M.; Dhinojwala, A. *Nano Lett.* **2008**, *8*, 822–825.
- (27) Geim, A. K.; Dubonos, S. V.; Grigorieva, I. V.; Novoselov, K. S.; Zhukov, A. A.; Shapoval, S. Y. *Nat. Mater.* **2003**, *2*, 461–463.
- (28) Glassmaker, N. J.; Jagota, A.; Hui, C. Y.; Kim, J. *J. R. Soc., Interface* **2004**, *1*, 23–33.
- (29) Majidi, C.; Groff, R. E.; Maeno, Y.; Schubert, B.; Baek, S.; Bush, B.; Maboudian, R.; Gravish, N.; Wilkinson, M.; Autumn, K.; Fearing, R. S. *Phys. Rev. Lett.* **2006**, *97*, 076103.
- (30) Kim, S.; Sitti, M. *Appl. Phys. Lett.* **2006**, *89*, 261911.
- (31) del Campo, A.; Greiner, C.; Alvarez, I.; Arzt, E. *Adv. Mater.* **2007**, *19*, 1973–1977.
- (32) Greiner, C.; del Campo, A.; Arzt, E. *Langmuir* **2007**, *23*, 3495–3502.
- (33) Kim, D. S.; Lee, H. S.; Lee, J.; Kim, S.; Lee, K. H.; Moon, W.; Kwon, T. H. *Microsyst. Technol.* **2007**, *13*, 601–606.
- (34) Murphy, M. P.; Aksak, B.; Sitti, M. *Small* **2009**, *5*, 170–175.
- (35) Murphy, M. P.; Kim, S.; Sitti, M. *ACS Appl. Mater. Interfaces* **2009**, *1*, 849–855.
- (36) Jeong, H. E.; Lee, J. K.; Kim, H. N.; Moon, S. H.; Suh, K. Y. *Proc. Natl. Acad. Sci. U.S.A.* **2009**, *106*, 5639–5644.
- (37) Gao, H. J.; Yao, H. M. *Proc. Natl. Acad. Sci. U.S.A.* **2004**, *101*, 7851–7856.
- (38) Kamperman, M.; Kroner, E.; del Campo, A.; McMeeking, R. M.; Arzt, E. *Adv. Eng. Mater.* **2010**, *12*, 335–348.
- (39) Qu, L. T.; Dai, L. M.; Stone, M.; Xia, Z. H.; Wang, Z. L. *Science* **2008**, *322*, 238–242.
- (40) Ge, L. H.; Ci, L. J.; Goyal, A.; Shi, R.; Mahadevan, L.; Ajayan, P. M.; Dhinojwala, A. *Nano Lett.* **2010**, *10*, 4509–4513.
- (41) Hu, S. H.; Jiang, H. D.; Xia, Z. H.; Gao, X. S. *ACS Appl. Mater. Interfaces* **2010**, *2*, 2570–2578.
- (42) Brenner, D. W.; Shenderova, O. A.; Harrison, J. A.; Stuart, S. J.; Ni, B.; Sinnott, S. B. *J. Phys.: Condens. Matter* **2002**, *14*, 783–802.
- (43) Pastewka, L.; Pou, P.; Perez, R.; Gumbsch, P.; Moseler, M. *Phys. Rev. B* **2008**, *78*, 161402.
- (44) Gao, G. T.; Mikulski, P. T.; Harrison, J. A. *J. Am. Chem. Soc.* **2002**, *124*, 7202–7209.
- (45) Li, L. L.; Xia, Z. H. H.; Curtin, W. A.; Yang, Y. Q. *J. Am. Ceram. Soc.* **2009**, *92*, 2331–2336.
- (46) Mo, Y. F.; Turner, K. T.; Szułfarska, I. *Nature* **2009**, *457*, 1116–1119.
- (47) Lucas, M.; Zhang, X. H.; Palaci, I.; Klinke, C.; Tosatti, E.; Riedo, E. *Nat. Mater.* **2009**, *8*, 876–881.
- (48) Pastewka, L.; Moser, S.; Gumbsch, P.; Moseler, M. *Nat. Mater.* **2011**, *10*, 34–38.
- (49) Ishikawa, M.; Harada, R.; Sasaki, N.; Miura, K. *Phys. Rev. B* **2009**, *80*, 193406.
- (50) Autumn, K.; Dittmore, A.; Santos, D.; Spenko, M.; Cutkosky, M. *J. Exp. Biol.* **2006**, *209*, 3569–3579.
- (51) Kendall, K. *J. Phys. D: Appl. Phys.* **1975**, *8*, 1449–1452.
- (52) Persson, B. N. J.; Gorb, S. *J. Chem. Phys.* **2003**, *119*, 11437–11444.
- (53) Chen, B.; Wu, P. D.; Gao, H. *Proc. R. Soc. A* **2008**, *464*, 1639–1652.
- (54) Tian, Y.; Pesika, N.; Zeng, H. B.; Rosenberg, K.; Zhao, B. X.; McGuiggan, P.; Autumn, K.; Israelachvili, J. *Proc. Natl. Acad. Sci. U.S.A.* **2006**, *103*, 19320–19325.
- (55) Chen, B.; Wu, P. D.; Gao, H. *J. R. Soc., Interface* **2009**, *6*, 529–537.
- (56) Schubert, B.; Lee, J.; Majidi, C.; Fearing, R. S. *J. R. Soc., Interface* **2008**, *5*, 845–853.